Spin-Orbit Effects on Exciton Complexes in Diamond

Shinya Takahashi, Yoshiki Kubo, Kazuki Konishi, Riadh Issaoui, Julien Barjon, Nobuko Naka

Spin-Orbit Effects on Exciton Complexes in Diamond

Shinya Takahashi,[1] Yoshiki Kubo,[1] Kazuki Konishi,[1] Riadh Issaoui,[2] Julien Barjon,[3] and Nobuko Naka[1,*]

[1] *Department of Physics, Kyoto University, Kitashirakawa-Oiwake-cho, Sakyo-ku, Kyoto, 606-8502, Japan*
[2] *LSPM-CNRS, Université Sorbonne Paris Nord, 99 Avenue Jean-Baptiste Clément, 93430 Villetaneuse, France*
[3] *GEMaC, Université de Versailles St-Quentin-en-Yvelines, CNRS, Université Paris-Saclay, 45 avenue des États-Unis, 78035 Versailles cedex, France*

(Dated: November 24, 2023)

Ultrafine splittings are found in the optical absorption spectra of boron-doped diamond measured with high resolution. An analytical model of an exciton complex is developed, which permits assigning all absorption lines and sizing the interactions among the constituent charges and crystal field. We conclude that the entry of split-off holes in the acceptor-bound exciton fine structure yields two triplets separated by a spin-orbit splitting of 14.3 meV. Our findings thereby resolve a long-standing controversy [Sauer *et al.* Phys. Rev. Lett. **84**, 4172 (2000), Cardona *et al.* Phys. Rev. Lett. **86**, 3923 (2001), Sauer *et al.* Phys. Rev. Lett. **86**, 3924 (2001)], revealing the underlying physics common in diverse semiconductors, including diamond.

Spin-orbit interaction arises from the relativistic effect of the spin angular momentum on valence electron orbitals, and its strength Δ varies with the atomic number, z, as $\Delta \propto z^4$. It is the basis for spintronics [1, 2] and various exotic concepts in solids and ultracold atoms, e.g., topological supersolids and quartet superfluids under artificial gauge fields [3, 4]. Combined with spin exchange interaction, it determines the energy structures of optical centers, formed around defects in a crystal lattice, and excitons, which are Coulomb-bound pairs of an electron and a hole. These energy structures critically impact the quantum emission yields [5–7] and spin readout fidelity of quantum sensors [8] formed of organic and inorganic crystals.

In analogy with the deuteron theory in nuclear physics [9, 10], the energy structures of excitons in semiconductors have been thoroughly investigated in terms of hole-hole *spin* exchange interaction on top of crystal-field interaction for more than 50 years [11–15]. However, the spin-orbit effect on excitons is not observed in classical semiconductors, such as silicon, germanium, and gallium arsenide, which have narrow bandgaps with cubic crystal structures. This is because the excessively large spin-orbit coupling of heavy atoms expels the split-off hole band, arising from the spin-orbit interaction, out of the excitonic fine structure of the smaller splitting. Contrastingly, the split-off hole band for excitons in wide-bandgap wurtzite-type semiconductors has been extensively considered [16–18]. Therefore, a large gap remains in the understanding between the two groups of semiconductors at the opposite extrema on the energy scale.

In this study, we investigated the fine structures of acceptor-bound excitons in diamond by considering the split-off characteristics of holes. We established a unified model of exciton complexes in semiconductors including silicon based on current industrial relevance and emerging materials for next-generation technologies where excitons dominate at room temperature. We used diamond, a key elemental semiconductor for low-consumption power devices and quantum technologies [8], to fill this gap, which has become important with the emergence of excitronics in two-dimensional materials [19, 20] and exciton Rydberg physics [21, 22]. Counterintuitively, the small spin-orbit coupling of light carbon atoms is ideal for exploring the role of split-off holes on excitons [23, 24], whose responses are far from the indirect bandgap of diamond at 5.5 eV [25, 26].

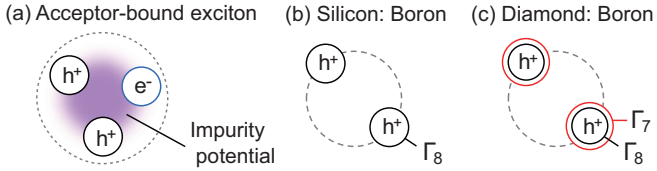

FIG. 1. (a) Four-body diagram of an acceptor-bound exciton, (b) conventional model describing an acceptor-bound exciton, considering only Γ_8 acceptor holes, and (c) our model introducing the split-off holes of Γ_7 symmetry.

Here we deal with a dopant site occupied by one exciton — an impurity-bound exciton. Theoretically, impurity-bound excitons are understood based on spin coupling of two particles of the same charge and an oppositely charged particle localized around the impurity potential [Fig. 1(a)]. When the impurity is an acceptor (e.g., boron in silicon), the model approximates the four-body bound state by considering the coupled states of the two holes in the top acceptor level [Fig. 1(b)]. The two holes reside in antisymmetric spin states with two different total angular momenta (J), reflecting their fermionic character. One of the J states further splits into two manifolds in the crystal field (exhibiting a symmetry lower than spherical), yielding a *triplet* bound-exciton structure in cubic semiconductors [11]. Experimentally, the triplet structure was decisively established for excitons bound to acceptors in silicon [12]. This crystal-field scheme based on two-hole states is the standard model for bound excitons in semiconductors [13–15].

Although diamond possesses cubic structure similar to silicon, the cathodoluminescence spectrum of boron-doped diamond exhibited a double quadruplet instead of a triplet [27, 28]. This observation, made 20 years ago, has excluded diamond from the common understanding of semiconductor physics, resulting in the strong ongoing debate [28–30]. The experimental challenges lie in the absence of absorption measurements on the bound exciton in diamond until recently, owing to the lack of appropriately doped samples [31]. Here, we report extra fine splittings found by improved spectral resolution, which support our crystal-field scheme including the split-off hole [red circles in Fig. 1(c)]. This closes the debate by demonstrating a unified description of the spin-orbit interaction in exciton complexes in semiconductors, as explained below.

Referring to the original crystal-field scheme [12], we used group theory to treat the energy levels in boron-doped diamond. The top valence band of diamond comprises two levels separated by approximately 6 meV through spin-orbit interaction [32]. After doping boron atoms at substitutional sites with carbon atoms, the symmetry is lowered to cubic without inversion [33]. Doping induces the formation of acceptor levels at approximately 360 meV above these valence bands. Reflecting the valence band splitting, the weakly bound hole of the acceptor splits into two levels with a reduced separation of 2 meV [Δ_a in Fig. 2(a)], as measured by electronic Raman spectroscopy [34] and confirmed later in this study. These acceptor levels are designated Γ_8 and Γ_7 using the irreducible representations of the tetrahedral point group, T_d. The level ordering is reversed in Fig. 2 compared to the usual energy diagram for electronic bands to represent the hole energy. The Γ_7 level is referred to as the split-off acceptor.

The electron of the acceptor-bound exciton resides in the conduction band, whereas two holes are located either at the Γ_8 or Γ_7 acceptor level. Therefore, the two-hole states of $\Gamma_8\otimes\Gamma_8$, $\Gamma_7\otimes\Gamma_8$, and $\Gamma_7\otimes\Gamma_7$ symmetries can arise from low to high energies [Fig. 2(b)], where the symbol $\otimes$ denotes the direct product of two irreducible representations. The splitting of the two-hole states by symmetry-breaking interactions is derived by treating the two holes quantum mechanically. We let $\hat{\boldsymbol{j}}_1$ and $\hat{\boldsymbol{j}}_2$ be the angular momentum operators for the holes; $j_1, j_2 = 3/2$ (or $1/2$) correspond to the Γ_8 (or Γ_7, split-off) acceptor levels. Similarly, $\hat{\boldsymbol{J}} = \hat{\boldsymbol{j}}_1 + \hat{\boldsymbol{j}}_2$ is the total angular momentum operator of the two-hole state. The coupling of $\hat{\boldsymbol{j}}_1$ and $\hat{\boldsymbol{j}}_2$ yields $J = (3), 2, (1), 0$ as derived from $\Gamma_8 \otimes \Gamma_8$, $J = 2, 1$ from $\Gamma_7 \otimes \Gamma_8$, and $J = (1), 0$ from $\Gamma_7 \otimes \Gamma_7$. The levels in parentheses are states of two identical fermions sharing the same angular momentum state, which are forbidden by Pauli's exclusion principle and therefore omitted in Fig. 2(c). The two-hole states range from low to high energies according to Hund's rule in atomic theory [35]. There are two $J = 2$ states, and each splits into a doublet

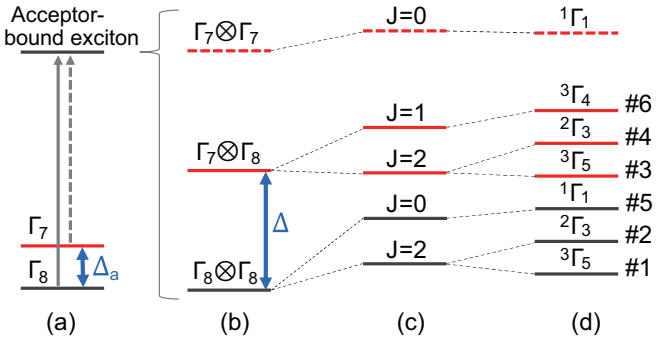

FIG. 2. (a) Schematic of absorption transitions from acceptor (Γ_8, Γ_7) to acceptor-bound exciton states. (b) Two-hole states extended for split-off (Γ_7) holes, including (c) hole-hole exchange interaction and (d) crystal-field splitting. Δ_a and Δ denote the spin-orbit splitting in the acceptor and bound exciton states, respectively. The split levels are shown not to scale and grouped in (d) by the triplet system, rather than energy ordering (#1−#6) in the measured spectra.

denoted by ${}^3\Gamma_5$ and ${}^2\Gamma_3$ under the T_d symmetry of the crystal field [Fig. 2(d)]. Here, the superscripts represent the dimension of the irreducible representations, that is, the degeneracy of the states. These level degeneracies were provisionally considered to indicate the absorption intensities in our level assignments in Table I.

To summarize the theory at this stage, we expect seven levels for acceptor-bound excitons. The fine structure in diamond is fundamentally more intricate than that in silicon, in which only a triplet from $\Gamma_8 \otimes \Gamma_8$ two-hole states is expected [black lines in Fig. 2(d)]. Another triplet ($\Gamma_7 \otimes \Gamma_8$) and singlet ($\Gamma_7 \otimes \Gamma_7$) are our first predictions, including the split-off acceptor, as indicated by the solid and dashed red lines. To compare with experiments probing absorption transitions, as shown in Fig. 2(a), we indexed the levels by numbers #1−#6 from low to high energies in the measured spectra.

Our strategy of measuring absorption is complementary to luminescence, and allows the direct estimation of relative oscillator strengths from the absorption intensities [12] without thermal broadening. The sample and equipment details can be found in Refs. [31, 36]. We additionally implemented a higher-resolution monochromator to achieve the best spectral resolution of 0.14 meV corresponding to a 6-fold improvement over our previous report [31]. Further details, including the elimination of interference fringes, chromatic aberration, and the background irrelevant to the bound excitons, are provided in Sec. I of the Supplemental Material [37].

The representative absorption spectra of boron-doped diamond at $6 - 160$ K are presented in Fig. 3(a). The high-temperature spectrum resembles those reported for cathodoluminescence [28]. Figure 3(b) shows the temperature (T) variation of the full width at half maximum (FWHM) of the highest energy peak (after deconvoluted

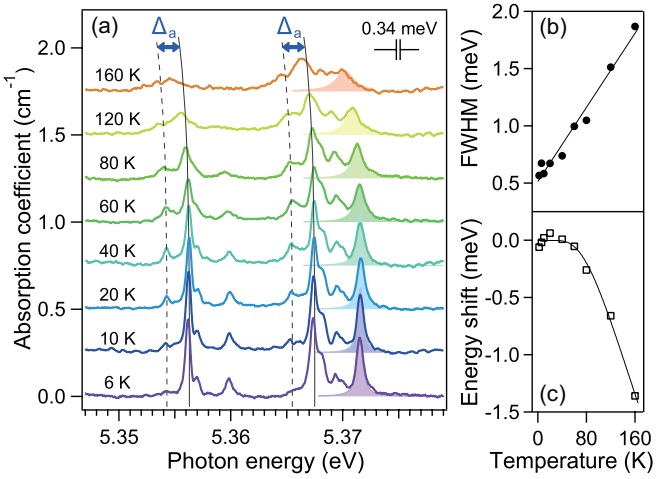

FIG. 3. (a) Absorption spectra of bound excitons in boron-doped diamond between 6 − 160 K. The dashed lines represent transitions from the upper acceptor level. (b) Temperature dependence of the Lorentzian width (FWHM) of line #6 [shaded in (a)]. (c) Temperature shift of line #6. The solid lines in (b) and (c) represent fit functions (see text).

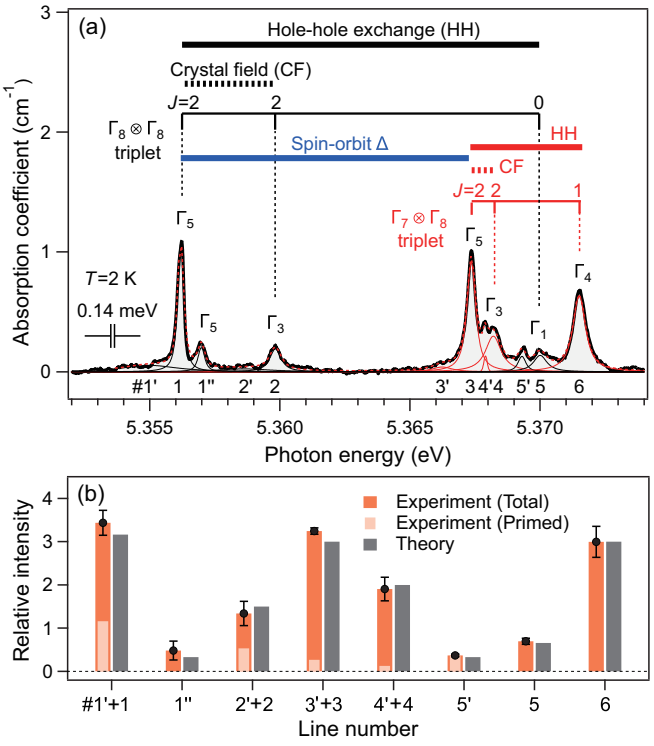

FIG. 4. (a) Higher-resolution absorption spectrum at 2 K (thick black line) fitted with the sum (dotted red line) of eleven Voigt functions, #1′−#6 (thin lines). The labels near the respective peaks represent the symmetry of the two-hole states. The brackets and horizontal bars at the top indicate two sets of triplets and the approximate size of the splittings, respectively. (b) Comparison of the experimental and theoretical absorption strengths. Orange bars with dots indicate the areal intensities of #1, #2, and #4 superposed on top of #1′, #2′, and #4′, respectively. Thinner bars indicate intensities of primed peaks. The theory (gray bars) includes the electron-hole exchange effect for lines #1′−#2 and valley-orbit splitting for #5′ and #5 (details in Sec. III of Supplemental Material [37]).

from the spectral resolution of detection) and a linear fit with 8.1 μeV/K. Figure 3(c) shows the energy shift δ of the same peak and a fit using $\delta(T) = -\dfrac{a\theta}{\exp(\theta/T)-1}$ [26], where $a = 11.0$ μeV/K and $\theta = 307$ K. As indicated by the dashed lines in Fig. 3(a), some of the peaks diminish with decreasing temperatures. We attribute them to the absorption transitions from the upper (Γ_7) acceptor level, which confirms that $\Delta_a = 2$ meV (details in Sec. II of the Supplemental Material [37]).

A higher-resolution spectrum obtained at 2 K is shown in Fig. 4(a), where the line numbers are indicated at the bottom. At least five lines ($\#1'', \#4', \#4, \#5', \#5$) are additionally resolved from only four lines ($\#1, \#2, \#3, \#6$) in our previous report [31]. We fit the spectrum with the sum of Voigt functions, that is, the sum of Lorentzian functions

$$\alpha_{\rm fit}(E) = \sum_i \frac{A_i}{\pi} \frac{2w_i}{4(E-E_i)^2 + w_i^2}, \qquad (1)$$

convoluted with a Gaussian function representing the spectral resolution of the detection system. After carefully examining the residual of the fit, the lines #1′, #2′, and #3′ were included to represent the weak components at the tails of #1, #2, and #3. Therefore, i denotes 1′, 1, 1″, 2′, 2, 3, 3′, 4′, 4, 5′, 5, and 6. A_i, w_i, and E_i denote the areal intensity, FWHM, and position of the peak, respectively. The best-fit functions for each peak are shown by thin lines. A comparison of the sum (dotted red line) with the data (thick black line) shows excellent agreement. The obtained fitting parameters are listed in Table I.

We attempted to assign the observed peaks to the respective bound-exciton levels by equating the intensities ($\tilde{A}_i$, obtained by normalizing A_i to a value of three for line #6) with the level degeneracies (g). The results are summarized in Table I, which yields fair (but incomplete) agreement between $\tilde{A}_i$ and g. A more complete model is presented in Sec. III in the Supplemental Material [37] by introducing subsidiary interactions, such as electron-hole exchange. Although only numerical solutions were considered previously [13], we found that the total interaction Hamiltonian has analytical solutions. We derived the eigenvalues E_i^* and relative oscillator strength $\tilde{A}_i^*$ of the dipole transitions using the atomic theory [35]. The theoretical strengths of lines #1 and #2 were found to deviate from g, depending on the ratio of the electron-hole exchange to crystal-field interaction parameters. This enabled the precise sizing of interaction parameters by fitting the measured spectrum to the analytically expressed

TABLE I. Results of the fitting of the spectrum in Fig. 4(a) to Eq. (1), compared with theory. E_i: peak energy, ΔE_i: separation from E_1, w_i: Lorentzian width (FWHM deconvoluted from the spectral resolution), A_i: areal intensity, $\tilde{A}_i$: areal intensity relative to line #6 taken as three, g: level degeneracy, S: irreducible representation of the two-hole states, J: total angular momentum, T: irreducible representations of the constituent hole states. $\tilde{A}_i^*$: relative oscillator strengths calculated using the interaction parameters extracted in Sec. III of the Supplemental Material [37].

Line	Experiment					Theory				
#	E_i [eV]	ΔE_i [meV]	w_i [meV]	A_i [meV(cm)$^{-1}$]	$\tilde{A}_i$	g	S	J	T	$\tilde{A}_i^*$
6	5.3715	15.3	0.54	0.567	3	3	Γ_4	1	$\Gamma_7 \otimes \Gamma_8$	3
5	5.3700	13.8	0.59	0.132	0.70	1	Γ_1	0	$\Gamma_8 \otimes \Gamma_8$	0.67
5′	5.3693	13.1	0.31	0.070	0.37					0.33
4	5.3682	12.0	0.70	0.336	1.78	2	Γ_3	2	$\Gamma_7 \otimes \Gamma_8$	} 2
4′	5.3679	11.7	0.03	0.024	0.13					
3	5.3674	11.2	0.36	0.562	2.98	3	Γ_5	2	$\Gamma_7 \otimes \Gamma_8$	} 3
3′	5.3662	10.0	0.82	0.051	0.27					
2	5.3598	3.6	0.48	0.152	0.80	2	Γ_3	2	$\Gamma_8 \otimes \Gamma_8$	} 1.50
2′	5.3586	2.4	2.58	0.100	0.53					
1″	5.3570	0.8	0.24	0.091	0.48					0.33
1	5.3562	0	0.21	0.430	2.28	3	Γ_5	2	$\Gamma_8 \otimes \Gamma_8$	} 3.17
1′	5.3550	−1.2	2.58	0.219	1.16					

$\alpha_{\rm fit}(E)$ using E_i^* and $\tilde{A}_i^*$ thus derived. The best-fit interaction parameters given in Table SIV of the Supplemental Material [37] yielded the theoretical strengths $\tilde{A}_i^*$ (including those for some primed peaks) in Table I. The remarkable agreement with the experimental intensities $\tilde{A}_i$ is presented in Fig. 4(b). This confirms the validity of our level assignments refined with the electron-hole exchange effect.

We observed that the fine structure follows the crystal-field scheme under the hole-hole exchange interaction [see horizontal bars in Fig. 4(a)]. The detailed attributions are as follows: Lines #1, #2, and #5 constitute the $\Gamma_8 \otimes \Gamma_8$ triplet. Lines #3, #4, and #6 constitute the $\Gamma_7 \otimes \Gamma_8$ (split-off) triplet, which was observed for the first time in cubic semiconductors. The transitions to the $\Gamma_7 \otimes \Gamma_7$ singlet were not observed despite the high sensitivity of our setup (see Fig. S3 in the Supplemental Material [37]). Lines #2 (#4) and #5 (#6) lift from the ground state of the triplet mainly by the crystal-field splitting of 3.3 (0.9) meV and hole-hole exchange splitting of 12.3 (3.8) meV, respectively, whose effects have never been quantitatively discussed for diamond. The interdigitation of the two triplets, compared with Hund's rule, is explained by the large hole-hole exchange splitting in the $\Gamma_8 \otimes \Gamma_8$ triplet.

The minor splitting of lines #1−#5 is considered the effects of coupling with the electron. We attribute the splitting of lines #1−#1″ to the electron-hole exchange interaction [13, 44] and other splittings to weak valley-orbit coupling as seen in boron-doped silicon [45, 46].

In luminescence studies [28, 30], the insufficient spectral resolution owing to instrumental and thermal broadening (typically 1 meV) led to a confusing interpretation attributing the separation between lines #1 and #3 to the electron-hole exchange splitting of two identical internal structures. Our high-resolution absorption data excluded this possibility, and we further separated the size and primary origin of the internal splitting: $|E_2 - E_1| = 3.6$ meV by the crystal-field effect in the $\Gamma_8 \otimes \Gamma_8$ triplet whereas $|E_6 - E_3| = 4.1$ meV by the hole-hole exchange in the $\Gamma_7 \otimes \Gamma_8$ triplet. The separation between the two triplets approximately provides the spin-orbit splitting. The refined value after removing the crystal-field and exchange energies by the least-squares fit was $\Delta = 14.3 \pm 0.1$ meV. This is the first accurate determination of the spin-orbit interaction parameter for acceptor-bound excitons in semiconductors. Consistently with the theoretical suggestions [47], this finding demonstrates that the spin-orbit splitting for the exciton complex in diamond is remarkably enhanced compared to that for the acceptor hole ($\Delta_{\rm a} = 2$ meV).

We further examined previously reported observations [12–16, 45, 48–57] using our unified model and directly compared the extracted splitting of narrow- and wide-bandgap materials (Table SV, Supplemental Material [37]). This provides the following general trends: i) hole-hole exchange interactions dominate in cubic semiconductors, ii) the $J = 2$ state forms the ground state of excitons bound to shallow acceptors, and iii) diamond is an extreme case of large energy splitting among cubic semiconductors. The split-off hole appears owing to the high localization energy, which occurs similarly in wide-bandgap semiconductors of hexagonal structures. This confluent view including split-off hole bands addresses the gap in modeling exciton complexes in semiconductors.

In summary, we applied an analytical model developed for the interacting charges that form exciton complexes to the ultrafine splittings observed in the absorption spectra of boron-doped diamond. We explained the acceptor-bound exciton fine structure in diamond by two interdig-

itated triplets, thereby resolving a long-standing debate. The experimental confirmation of the lift of level degeneracies under external fields is an interesting future work. Highlighting the shared underlying physics among semiconductors, our findings may deepen understanding of the spin-orbit effects and symmetry breaking in systems such as nontrivial few-body bound states [4, 20]. Our new knowledge of the fundamental properties of doped diamond also provides insights for future technologies beyond silicon, where excitons govern the optical properties at room temperature.

This work is partially supported by JSPS KAKENHI Grants JP17H02910 and JP21K03420, and PICS (Grant No. 200835) from Centre National de la Recherche Scientifique, France.

* naka@scphys.kyoto-u.ac.jp

[1] L. Sun, L. Rademaker, D. Mauro, A. Scarfato, A. Pásztor, I. Gutiérrez-Lezama, Z. Wang, J. Martinez-Castro, A. F. Morpurgo, and C. Renner, Determining spin-orbit coupling in graphene by quasiparticle interference imaging, Nat. Commun. **14**, 3771 (2023).

[2] S. Lee, H. Koike, M. Goto, S. Miwa, Y. Suzuki, N. Yamashita, R. Ohshima, E. Shigematsu, Y. Ando, and M. Shiraishi, Synthetic Rashba spin-orbit system using a silicon metal-oxide semiconductor, Nat. Mater. **20**, 1228 (2021).

[3] G. I. Martone and N. Cherroret, Time Translation Symmetry Braking in an Isolated Spin-Orbit-Coupled Fluid of Light, Phys. Rev. Lett. **131**, 013803 (2023).

[4] R. Liu, W. Wang, and X. Cui, Quartet Superfluid in Two-Dimensional Mass-Imbalanced Fermi Mixtures, Phys. Rev. Lett. **131**, 193401 (2023).

[5] X. He, H. Htoon, S. K. Doorn, W. H. P. Pernice, F. Pyatkov, R. Krupke, A. Jeantet, Y. Chassagneux, and C. Voisin, Carbon nanotubes as emerging quantum-light sources, Nat. Mater. **17**, 663 (2018).

[6] K. Zollner, M. Gmitra, and J. Fabian, Swapping Exchange and Spin-Orbit Coupling in 2D van der Waals Heterostructures, Phys. Rev. Lett. **125**, 196402 (2020).

[7] D. Weinberg, Y. Park, D. T. Limmer, and E. Rabani, Size-Dependent Lattice Symmetry Breaking Determines the Exciton Fine Structure of Perovskite Nanocrystals, Nano Lett. **23**, 4997 (2023).

[8] S. Ernst, P. J. Scheidegger, S. Diesch, L. Lorenzelli, and C. L. Degen, Temperature Dependence of Photoluminescence Intensity and Spin Contrast in Nitrogen-Vacancy Centers, Phys. Rev. Lett. **131**, 086903 (2023).

[9] E. I. Rashba and G. E. Gurgenishvili, Edge Absorption Theory in Semiconductors, Sov. Phys. - Solid State **4**, 759 (1962).

[10] H. Bethe and R. Peierls, Quantum theory of the diplon, Proc. R. Soc. London. Ser. A - Math. Phys. Sci. **148**, 146 (1935).

[11] P. J. Dean and D. C. Herbert, Bound Excitons in Semiconductors, in *Excitons* (1979) pp. 55–182.

[12] K. R. Elliott, G. C. Osbourn, D. L. Smith, and T. C. McGill, Bound-exciton absorption in Si:Al, Si:Ga, and Si:In, Phys. Rev. B **17**, 1808 (1978).

[13] E. Molva and L. S. Dang, Magneto-optical study of Li and Na acceptor bound excitons in CdTe: Fine structure and cubic crystal-field effect, Phys. Rev. B **32**, 1156 (1985).

[14] H. Mathieu, J. Camassel, and F. B. Chekroun, Stress effects on excitons bound to neutral acceptors in InP, Phys. Rev. B **29**, 3438 (1984).

[15] M. Schmidt, T. N. Morgan, and W. Schairer, Stress effects on excitons bound to shallow acceptors in GaAs, Phys. Rev. B **11**, 5002 (1975).

[16] B. Gil, P. Bigenwald, P. P. Paskov, and B. Monemar, Internal structure of acceptor-bound excitons in wide-bandgap wurtzite semiconductors, Phys. Rev. B **81**, 085211 (2010).

[17] B. K. Meyer, J. Sann, S. Eisermann, S. Lautenschlaeger, M. R. Wagner, M. Kaiser, G. Callsen, J. S. Reparaz, and A. Hoffmann, Excited state properties of donor bound excitons in ZnO, Phys. Rev. B **82**, 115207 (2010).

[18] G. Callsen, T. Kure, M. R. Wagner, R. Butté, and N. Grandjean, Excited states of neutral donor bound excitons in GaN, J. Appl. Phys. **123**, 215702 (2018).

[19] G. Wang, A. Chernikov, M. M. Glazov, T. F. Heinz, X. Marie, T. Amand, and B. Urbaszek, Colloquium: Excitons in atomically thin transition metal dichalcogenides, Rev. Mod. Phys. **90**, 021001 (2018).

[20] D. V. Tuan, S.-F. Shi, X. Xu, S. A. Crooker, and H. Dery, Six-Body and Eight-Body Exciton States in Monolayer WSe_2, Phys. Re. Lett. **129**, 076801 (2023).

[21] T. Kazimierczuk, D. Fröhlich, S. Scheel, H. Stolz, and M. Bayer, Giant Rydberg excitons in the copper oxide Cu_2O, Nature **514**, 343 (2014).

[22] M. Assmann and M. Bayer, Semiconductor Rydberg Physics, Adv. Quantum Technol. **3**, 1900134 (2020).

[23] Y. Hazama, N. Naka, and H. Stolz, Mass-anisotropy splitting of indirect excitons in diamond, Phys. Rev. B **90**, 045209 (2014).

[24] T. Ichii, N. Naka, and K. Tanaka, Rotational symmetry breaking on the Rydberg energy spectrum of indirect excitons in diamond studied by terahertz time-domain spectroscopy, Phys. Rev. B **104**, 205201 (2021).

[25] C. D. Clark, P. J. Dean, and P. V. Harris, Intrinsic edge absorption in diamond, Proc. R. Soc. London. Ser. A. Math. Phys. Sci. **277**, 312 (1964).

[26] K. Konishi and N. Naka, Phonon-assisted excitonic absorption in diamond, Phys. Rev. B **104**, 125204 (2021).

[27] S. J. Sharp, A. T. Collins, G. Davies, and G. S. Joyce, Higher resolution studies of shallow bound exciton luminescence in diamond, J. Phys. Condens. Matter **9**, L451 (1997).

[28] R. Sauer, H. Sternschulte, S. Wahl, K. Thonke, and T. R. Anthony, Revised Fine Splitting of Excitons in Diamond, Phys. Rev. Lett. **84**, 4172 (2000).

[29] M. Cardona, T. Ruf, and J. Serrano, Comment on "Revised Fine Splitting of Excitons in Diamond", Phys. Rev. Lett. **86**, 3923 (2001).

[30] R. Sauer and K. Thonke, Sauer and Thonke Reply, Phys. Rev. Lett. **86**, 3924 (2001).

[31] Y. Kubo, S. Temgoua, R. Issaoui, J. Barjon, and N. Naka, Radiative lifetime of boron-bound excitons in diamond, Appl. Phys. Lett. **114**, 132104 (2019).

[32] C. J. Rauch, Millimeter Cyclotron Resonance Experiments in Diamond, Phys. Rev. Lett. **7**, 83 (1961).

[33] P. Y. Yu and M. Cardona, *Fundamentals of Semiconduc-*

tors (Springer, 2010).
[34] H. Kim, R. Vogelgesang, A. K. Ramdas, S. Rodriguez, M. Grimsditch, and T. R. Anthony, Electronic Raman and infrared spectra of acceptors in isotopically controlled diamonds, Phys. Rev. B **57**, 15315 (1998).
[35] E. U. Condon and G. H. Shortley, *The Theory of Atomic Spectra* (Cambridge University Press, 1963).
[36] R. Issaoui, J. Achard, A. Tallaire, F. Silva, A. Gicquel, R. Bisaro, B. Servet, G. Garry, and J. Barjon, Evaluation of freestanding boron-doped diamond grown by chemical vapour deposition as substrates for vertical power electronic devices, Appl. Phys. Lett. **100**, 122109 (2012).
[37] See the Supplemental Material at http://link.aps.org/supplemental/xxx for experimental details, temperature dependence, and a description of our theory, which includes Refs. [38–43].
[38] D. G. Thomas and J. J. Hopfield, Optical Properties of Bound Exciton Complexes in Cadmium Sulfide, Phys. Rev. **128**, 2135 (1962).
[39] S. Sugano, Y. Tanabe, and H. Kamimura, *Multiplets of Transition-Metal Ions in Crystals* (Academic Press, 1970).
[40] G. F. Koster, J. O. Dimmock, R. G. Wheeler, and H. Statz, *Properties of the thirty-two point groups* (MIT Press, 1963).
[41] T. Morgan, Oscillator strengths for electron-hole complexes (A^0X), J. Phys. C: Solid State Phys. **10**, L131 (1977).
[42] B. Hönerlage and I. Pelant, *Symmetry and Symmetry-Breaking in Semiconductors*, PUBDB-2021-02091 (Springer, 2018).
[43] Y. Kubo, M. Takahata, S. Temgoua, R. Issaoui, J. Barjon, and N. Naka, Phonon-assisted transitions of bound excitons in diamond: Analysis by mirror symmetry, Phys. Rev. B **101**, 205204 (2020).
[44] G. E. Pikus and G. L. Bir, Exchange Interaction In Excitons In Semiconductors, Sov. Phys. JETP **33**, 108 (1971).
[45] V. A. Karasyuk, A. G. Steele, A. Mainwood, E. C. Lightowlers, G. Davies, D. M. Brake, and M. L. W. Thewalt, Ultrahigh-resolution photoluminescence studies of excitons bound to boron in silicon under uniaxial stress, Phys. Rev. B **45**, 11736 (1992).
[46] A. Yang, M. Steger, T. Sekiguchi, D. Karaiskaj, M. L. W. Thewalt, M. Cardona, K. M. Itoh, H. Riemann, N. V. Abrosimov, M. F. Churbanov, A. V. Gusev, A. D. Bulanov, I. D. Kovalev, A. K. Kaliteevskii, O. N. Godisov, P. Becker, H.-J. Pohl, J. W. Ager, and E. E. Haller, Single-frequency laser spectroscopy of the boron bound exciton in ^{28}Si, Phys. Rev. B **80**, 195203 (2009).
[47] J. Serrano, M. Cardona, and T. Ruf, Spin-orbit splitting in diamond: excitons and acceptor related states, Solid State Commun. **113**, 411 (1999).
[48] O. Madelung, *Semiconductors: Data Handbook* (Springer, 2004).
[49] T. Shimomura, Y. Kubo, J. Barjon, N. Tokuda, I. Akimoto, and N. Naka, Quantitative relevance of substitutional impurities to carrier dynamics in diamond, Phys. Rev. Mater. **2**, 094601 (2018).
[50] A. Baldereschi and N. O. Lipari, Spherical Model of Shallow Acceptor States in Semiconductors, Phys. Rev. B **8**, 2697 (1973).
[51] J. Barjon, Luminescence Spectroscopy of Bound Excitons in Diamond, Phys. Status Solidi A **214**, 1700402 (2017).
[52] M. Vouk and E. Lightowlers, A high resolution investigation of the recombination radiation from Si containing the acceptors B, Al, Ga, In and Tl, J. Lumin. **15**, 357 (1977).
[53] Y. Takeuchi, Y. Makita, K. Kudo, T. Nomura, H. Tanaka, K. Irie, and N. Ohnishi, Observation of new common emissions in GaAs produced by ion implantation of four acceptor impurities, Appl. Phys. Lett. **48**, 59 (1986).
[54] J. Gutowski, Electronic and vibronic states of the acceptor—bound-exciton complex (A^0, X) in CdS. II. Determination of the fine structure of the (A^0, X_B) electronic states by high-resolution excitation spectroscopy, Phys. Rev. B **31**, 3611 (1985).
[55] A. Wysmolek, M. Potemski, R. Stepniewski, J. Lusakowski, K. Pakula, J. M. Baranowski, J. Martinez, P. Wyder, I. Grzegory, and S. Porowski, Polarised Magnetoluminescence of Excitons in Homoepitaxial GaN Layers, Phys. Status Solidi B **216**, 11 (1999).
[56] R. Ishii, A. Yoshikawa, M. Funato, and Y. Kawakami, Revisiting the substitutional Mg acceptor binding energy of AlN, Phys. Rev. B **108**, 035205 (2023).
[57] T. Karin, R. J. Barbour, C. Santori, Y. Yamamoto, Y. Hirayama, and Kai-Mei C. Fu, Radiative properties of multicarrier bound excitons in GaAs, Phys. Rev. B **91**, 165204 (2015).

Supplemental Material
Spin-Orbit Effects on Exciton Complexes in Diamond

Shinya Takahashi,[1] Yoshiki Kubo,[1] Kazuki Konishi,[1] Riadh Issaoui,[2] Julien Barjon,[3] and Nobuko Naka[1,*]

[1] *Department of Physics, Kyoto University, Kitashirakawa-Oiwake-cho, Sakyo-ku, Kyoto, 606-8502, Japan*
[2] *LSPM-CNRS, Université Sorbonne Paris Nord, 99 Avenue Jean-Baptiste Clément, 93430 Villetaneuse, France*
[3] *GEMaC, Université de Versailles St-Quentin-en-Yvelines, CNRS, Université Paris-Saclay, 45 avenue des États-Unis, 78035 Versailles cedex, France*

I. EXPERIMENTAL DETAILS

A. High-resolution absorption spectroscopy

We used a single-crystal diamond grown by plasma-assisted chemical vapor deposition as the sample, whose boron concentration was 1.8×10^{18} atoms/cm^3 [1]. The sample was cooled in a closed-cycle helium-gas cryostat down to 6 K or in a helium immersion cryostat at 2 K. Ultraviolet light from a deuterium lamp was transmitted through the sample and dispersed by a high-resolution monochromator (Jobin Yvon, THR1500) of a long focal length (1500 mm) equipped with a diffraction grating of 2400 grooves/mm. The signal was detected at a UV-enhanced charge-coupled-device (CCD) silicon camera of a small pixel size (13.5 μm) mounted at the exit port of the monochromator.

The indirect band gap of diamond is approximately 5.50 eV, which corresponds to a wavelength of 226 nm in the deep ultraviolet (UV) region. Achieving an energy resolution higher than 1 meV is a challenge in such a short wavelength extreme, as the same wavelength difference gives a larger energy difference at a shorter wavelength. For example, 1 nm difference corresponds to $\sim$20 meV at 250 nm while $\sim$5 meV at 500 nm. Therefore, the center wavelength was set at twice the target wavelength corresponding to second-order diffraction for measurements at 2 K. Our setting leads to roughly $2^4\times$ improvement of the reciprocal linear dispersion per pixel, compared to a standard high-resolution setup with, e.g., 750 mm focal length, 1200 grooves/mm grating, 27 μm pixel size, and first-order diffraction. To remove the visible component entering the second-order diffraction of the deep UV light, we loosely monochromatized the incident light from the deuterium lamp by using two dichroic mirrors (reflection for 248$\pm$30 nm), a harmonic separator (reflection from 205 to 240 nm), and a Pellin Broca prism. The spectral dispersion was 1.5 pm (0.035 meV) between two adjacent pixels of the camera.

The monochromator was fully covered by 30 mm-thick thermal insulation for temperature stabilization. With this passive stabilization, a slight shift of the center wavelength owing to the refractive index change of the air induced by the small temperature shift was observed in a reference experiment using a neon lamp. We analyzed the position of line #1 in the transmission spectra of each exposure of typically 450 sec. The shift was corrected when we take the average of the spectra accumulated multiple times. The total exposure time was 19 hours for the spectrum shown in Fig. 4(a) of the main text. The spectral resolution of 0.14 meV was achieved for measurements at 2 K at 15 μm-entrance slit width, as determined as the full width at half the maximum (FWHM) of the mercury line at 230.2768 nm in vacuum wavelength. This corresponds to a 6-fold improvement over our previous work [2] with 0.84 meV spectral resolution, and enabled resolving of 11 lines in the observed spectra. The Lorentzian width, w_i in Table I of the main text, has different values depending on the peaks, implying that some of them have further unresolved splitting. For higher temperature data, the monochromator was set at the first-diffraction mode and the spectral resolution at 50 μm slit width was 0.34 meV (FWHM). Note the difference of the spectral dispersion and resolution, which is sometimes overlooked in literature.

B. Baseline subtraction

The extrinsic absorption due to the no-phonon transition of the bound exciton in diamond is very weak. Therefore, usually neglected subtle effects, such as interference fringes and chromatic aberration, should be carefully treated. An absorption spectrum is obtained based on the transmission of light through a sample (i.e., signal), relative to the reference spectrum of incoming light. To increase the light intensity passing through the aperture in the sample holder, we focused the incident beam using an achromat lens. In the deep UV region, however, a slight chromatic aberration is unavoidable, which causes insubstantial differences in the spectra of incoming light through different apertures for the signal and reference.

Meanwhile, the interference fringes appear due to the difference in the coherency of signal and reference lights. Under the 6$-$160 K measurement condition, the fringe interval was only twice the spectral resolution of the detection system, and removal of the fringes by Fourier filtering or by sinusoidal fits to the baseline (as done for 2 K) was not possible. To compensate for decoherence occurring through the boron-doped sample of thickness $\ell = 0.251$ mm, using an intrinsic diamond of thickness

* naka@scphys.kyoto-u.ac.jp

$l_i = 0.532$ mm as a reference instead of vacuum was found to be effective [see Fig. S1(a)].

Therefore, we take the ratio of the transmittance through the boron-doped and intrinsic samples, $\mathcal{T}_{\rm sig}(E)$ and $\mathcal{T}_{\rm ref}(E)$, measured as a function of the photon energy E. Ideally, the ratio $\mathcal{T}(E) = \mathcal{T}_{\rm sig}(E)/\mathcal{T}_{\rm ref}(E)$ should be unity at a photon energy sufficiently below the band gap of diamond, where no absorption is expected. Therefore, we normalize $\mathcal{T}(E)$ by the value $\mathcal{T}_0 = \mathcal{T}(E = 5.30\ \text{eV})$. Including the multiple reflections and absorption in the samples, $\mathcal{T}(E)/\mathcal{T}_0$ is expressed as a quadratic equation of $\exp(-\alpha\ell - \alpha_{\rm i}\ell)$ [3], where $\alpha(E)$ and $\alpha_{\rm i}(E)$ are absorption coefficients of extrinsic and intrinsic origins, respectively, and the E-dependency is omitted in the notation. Based on the solution of the quadratic equation, we derived the relation

$$\alpha + \alpha_{\rm i} \simeq -\frac{1}{\ell}\ln\left(\frac{C(E)\exp(-\alpha_{\rm i} l_{\rm i})}{1 - R^2\exp\left(-2\alpha_{\rm i} l_{\rm i}\right)}\frac{\mathcal{T}(E)}{\mathcal{T}_0}\right),$$

where $R = 0.21$ is the reflectivity, assumed to be the same constant for doped and intrinsic samples, and $C(E)$ is an unknown function to account for the spectral difference in the signal and reference, caused by aberration.

The above relation means that the coefficient of extrinsic absorption due to the bound exciton can be expressed as

$$\alpha(E) \simeq -\frac{1}{\ell}\ln\frac{\mathcal{T}(E)}{\mathcal{T}_0} - B(E),$$

where the effects of aberration and intrinsic absorption are included in the baseline,

$$B(E) = \frac{1}{\ell}\ln\frac{C(E)\exp(-\alpha_{\rm i} l_{\rm i})}{1 - R^2\exp\left(-2\alpha_{\rm i} l_{\rm i}\right)} + \alpha_{\rm i}.$$

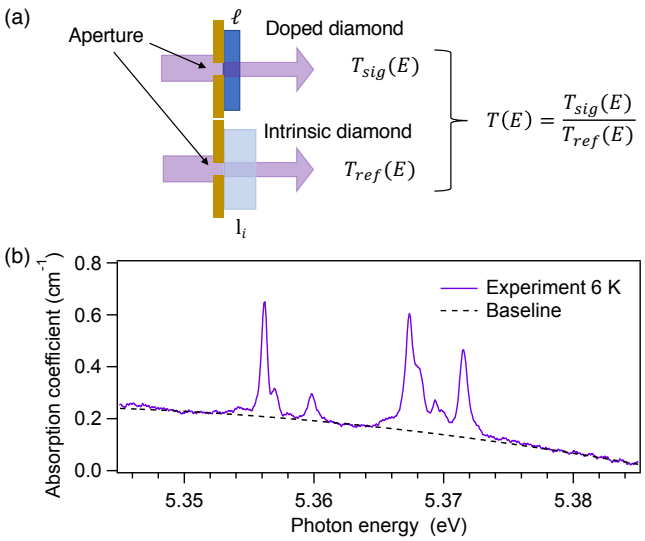

FIG. S1. (a) Schematic of measurement principle for transmission through boron-doped and intrinsic diamond samples. (b) Spectrum of $-(1/\ell)\ln[\mathcal{T}(E)/\mathcal{T}_0]$ at 6 K (solid line) and the baseline $B(E)$ (dashed line).

We approximate the baseline by a polynomial function: $B(E) = a + bE + cE^2$, considering that it depends only weakly on E in the transparent region of the free-exciton absorption spectrum [4]. An example of the baseline to a spectrum, obtained by a fit excluding the peaks, is shown in Fig. S1(b). Note that both $\ell^{-1}\ln\mathcal{T}_0$ and $B(E)$ are found to be minuscule (< 0.3 cm^{-1}), and thereby omitted in the expression in the main text for simplicity.

II. TEMPERATURE DEPENDENCE

As explained in the main text, absorption peaks at temperatures higher than 10 K consist of two components: transitions from the lower Γ_8 acceptor level and those from the upper Γ_7 acceptor level [2]. Here, we analyze the spectra obtained at various temperatures to provide an understanding consistent with the previously reported acceptor splitting, $\Delta_{\rm a} = 2$ meV [5].

We assume that each component contains lines #1−#6 as given by Eq. (1) in the main text (but omitting lines #1′, #2′, and #3′ of small peak heights). All peaks at 2 K are considered transitions from the Γ_8 acceptor level and directly reflect the fine structure of the bound exciton states. Provided that oscillator strengths are independent of the detailed shape of the wavefunctions, an absorption strength is expected to be proportional to the initial population in the respective acceptor levels. Therefore, we take a weighted sum of the two compo-

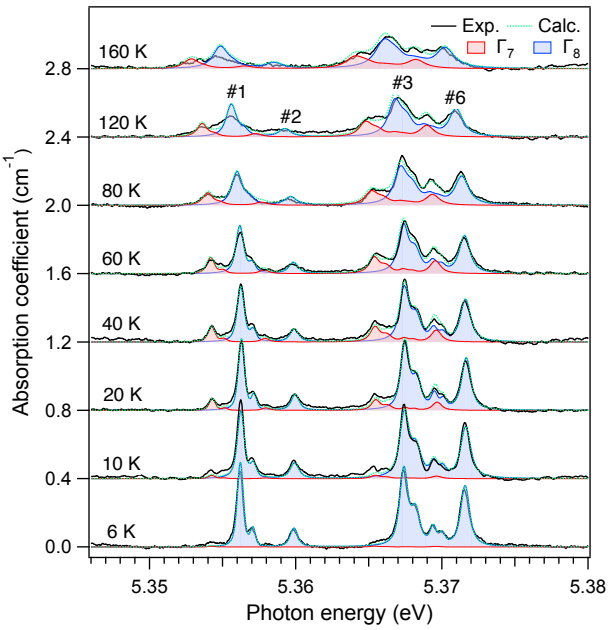

FIG. S2. (a) Absorption spectra of boron-doped diamond from 6 to 160 K. Measured spectra (black lines) are compared with the sum (dotted green lines), calculated for the transitions from the Γ_8 (blue lines) and Γ_7 (red lines) acceptor levels. Spectral broadening by the detection system was included in the calculation.

nents for the spectral function:

$$\alpha_{\rm all}(E,T) = f(T')\alpha_{\rm fit}(E+\delta) * L(E,T) + [1-f(T')]\alpha_{\rm fit}(E+\delta-\Delta_{\rm a}) * L(E,T),$$

where $f(T') = g_{\rm l}\{g_{\rm l} + g_{\rm u}\exp[-\Delta_{\rm a}/(k_{\rm B}T')]\}^{-1}$ represents the fraction of initial distribution at the lower (Γ_8) acceptor level following the Boltzmann statistics. T' is the carrier temperature, which is found to be higher by 4 K than the base temperature T of the cryostat. $g_{\rm l}/g_{\rm u} = 2$ denotes the degeneracy ratio of the lower to upper acceptor levels separated by $\Delta_{\rm a}$. δ is the temperature-dependent energy shift, as shown in Fig. 3(c) of the main text. $*L(E,T)$ means to perform convolution by a Lorentzian function to include the homogeneous broadening owing to phonon scattering. This was effectively done by increasing the Lorentzian width by the amount extracted from line #6 [Fig. 3(b) of the main text].

We calculated $\alpha_{\rm all}(E,T)$ at respective temperatures and further convoluted them with a Gaussian function representing the broadening by the detection system. The results are shown by the dotted green lines in Fig. S2, which indicate excellent agreement with the experimental data (black lines). The red and blue lines indicate components originated from the lower (Γ_8) and upper (Γ_7) acceptor levels, respectively. The Γ_7 component at ~ 5.354 eV is the transition from the Γ_7 acceptor to the bound exciton derived from the $\Gamma_8 \otimes \Gamma_8$ two-hole states, which is considered to be forbidden if the flip of the hole spin is not allowed. Similar hole relaxation had been discussed in Ref. [6] and clarification of the mechanism is left for future study.

The high-temperature spectra resemble the double quadruplet reported for cathodoluminescence [7], as they consist of major four lines (#1, #2, #3, #6) and their Γ_7 counterparts.

III. THEORY FOR THE BOUND-EXCITON MODEL

Here, we present our more complete model including the spin-orbit, hole-hole exchange, crystal-field potential, and electron-hole exchange interactions on the bound exciton. It should be noted that not only the energy positions of the absorption lines but also the intensities may depend on the interaction strengths. This enables sizing the electron-hole interaction strength with an accuracy never reached so far for diamond. It is also noteworthy that bound-exciton structure in diamond had never been analyzed under the crystal-field scheme and thus we provide the values of crystal-field and hole-hole exchange splittings for the first time.

In the following, we show that the interaction Hamiltonian for the crystal-field potential plus electron-hole exchange can be block diagonalized and the secular equation has analytical solutions. After deriving the analytical forms of energies and oscillator strengths, we determine the size of each interaction parameter based on a fitting to simultaneously reproduce the experimental line positions and absorption intensities. We set $\hbar = 1$ throughout the section.

A. Energy positions

The spin-orbit interaction Hamiltonian for electron bands is expressed as

$$H_{\rm so} = \frac{2\Delta}{3}\hat{\boldsymbol{L}}\cdot\hat{\boldsymbol{s}}, \tag{S1}$$

where Δ is the interaction parameter defining the coupling strength, and $\hat{\boldsymbol{L}}$ and $\hat{\boldsymbol{s}}$ are orbital and spin angular momentum operator, respectively. This interaction on a hole with $L = 1$ and $s = 1/2$ yields an energy shift of $\Delta/3$ for the $|\hat{\boldsymbol{L}} + \hat{\boldsymbol{s}}| = j = 3/2$ band and $-2\Delta/3$ for the $|\hat{\boldsymbol{L}} + \hat{\boldsymbol{s}}| = j = 1/2$ (split-off) band, respectively. When considering the hole energy instead of electron energy, one obtains an energy shift of $-2\Delta/3$ for the $\Gamma_8 \otimes \Gamma_8$ two-hole states, $\Delta/3$ for the $\Gamma_7 \otimes \Gamma_8$ two-hole states, and $4\Delta/3$ for the $\Gamma_7 \otimes \Gamma_7$ two-hole states.

The split-off holes can be safely neglected only when the localization energy of excitons is small compared to the spin-orbit interaction. In such a case (like silicon), the contributions are dominated by the stronger transitions by free excitons or band-to-band involving the light- and heavy-hole bands.

We denote the spherical hole-hole exchange interaction Hamiltonian [8] by

$$H_{\rm hh} = \Xi\hat{\boldsymbol{j}}_1\cdot\hat{\boldsymbol{j}}_2 = \Xi(\hat{\boldsymbol{J}}^2 - \hat{\boldsymbol{j}}_1^2 - \hat{\boldsymbol{j}}_2^2)/2, \tag{S2}$$

where Ξ is the interaction parameter, j_1, $j_2 = 3/2$ or $1/2$, and $\hat{\boldsymbol{J}} = \hat{\boldsymbol{j}}_1 + \hat{\boldsymbol{j}}_2$. Hereafter, we use subscripts of 0, 1, and 2 to distinguish between the different two-hole states. Then, $H_{\rm hh}$ yields energy shifts of $-3\Xi_0/4$ and $-15\Xi_0/4$ for the $J = 2$ and $J = 0$ states of the $\Gamma_8 \otimes \Gamma_8$ triplet, $+3\Xi_1/4$ and $-5\Xi_1/4$ for the $J = 2$ and $J = 1$ states of the $\Gamma_7 \otimes \Gamma_8$ triplet, and $-3\Xi_2/4$ for the $J = 0$ state of the $\Gamma_7 \otimes \Gamma_7$ singlet, respectively.

The interaction Hamiltonian by crystal-field potential of strength ξ on the $J = 2$ states takes the matrix form

$$H_{\rm cf} = \xi \begin{array}{c} \\ |-2\rangle \\ |-1\rangle \\ |0\rangle \\ |+1\rangle \\ |+2\rangle \end{array} \begin{array}{c} \begin{array}{ccccc} |-2\rangle & |-1\rangle & |0\rangle & |+1\rangle & |+2\rangle \end{array} \\ \begin{pmatrix} 1/4 & 0 & 0 & 0 & 5/4 \\ 0 & -1 & 0 & 0 & 0 \\ 0 & 0 & 3/2 & 0 & 0 \\ 0 & 0 & 0 & -1 & 0 \\ 5/4 & 0 & 0 & 0 & 1/4 \end{pmatrix} \end{array}, \tag{S3}$$

for $J_z = -2, -1, 0, +1, +2$ bases in this order. This form of potential is known for an electron in a d-orbital [9], and commonly used for the analysis of bound excitons in III-V compounds [10]. The eigenvalues of $H_{\rm cf}$ are $-\xi$ and $3\xi/2$. Note that the same energy shifts can be derived from a different theoretical approach, i.e., by the cubic correction term $\sum_{i=x,y,z}\left(\hat{j}_{1i}^3\hat{j}_{2i} + \hat{j}_{1i}\hat{j}_{2i}^3\right)$ in the hole-hole exchange Hamiltonian with the method of invariants. This

approach is more commonly used for bound excitons in silicon [11] and for free excitons [12], and indicates that no splitting arises in the $J = 1$ and $J = 0$ states by the crystal-field interaction.

The electron-hole exchange interaction Hamiltonian in spherical approximation (neglecting the cubic corrections [11]) is expressed as

$$H_{\rm eh} = \gamma \hat{\boldsymbol{J}} \cdot \hat{\boldsymbol{s}} = \gamma \left[\left(\hat{J}_+ \hat{s}_- + \hat{J}_- \hat{s}_+ \right) /2 + \hat{J}_z \hat{s}_z \right], \quad \text{(S4)}$$

where γ is the interaction parameter, $\hat{\boldsymbol{J}}$ and $\hat{\boldsymbol{s}}$ are angular momentum operators of the two-hole and electron states, respectively, and $\hat{J}_\pm = \hat{J}_x \pm i\hat{J}_y$ and $\hat{s}_\pm = \hat{s}_x \pm i\hat{s}_y$ are ladder operators. By using the relation $\hat{J}_\pm |J, J_z\rangle = \sqrt{J(J+1) - J_z(J_z \pm 1)}\, |J, J_z \pm 1\rangle$ and $\hat{s}_\pm |s, s_z\rangle = \sqrt{s(s+1) - s_z(s_z \pm 1)}\, |s, s_z \pm 1\rangle$, we obtain the Hamiltonian of the form

$$H_{\rm eh} = \gamma \begin{array}{c} \begin{array}{cccccccccc} |-2;\downarrow\rangle & |-1;\downarrow\rangle & |0;\downarrow\rangle & |+1;\downarrow\rangle & |+2;\downarrow\rangle & |-2;\uparrow\rangle & |-1;\uparrow\rangle & |0;\uparrow\rangle & |+1;\uparrow\rangle & |+2;\uparrow\rangle \end{array} \\ \begin{pmatrix} 1 & & & & & & & & & \\ & 1/2 & & & & 1 & & & & \\ & & 0 & & & & \sqrt{6}/2 & & & \\ & & & -1/2 & & & & \sqrt{6}/2 & & \\ & & & & -1 & & & & 1 & \\ & 1 & & & & -1 & & & & \\ & & \sqrt{6}/2 & & & & -1/2 & & & \\ & & & \sqrt{6}/2 & & & & 0 & & \\ & & & & 1 & & & & 1/2 & \\ & & & & & & & & & 1 \end{pmatrix} \end{array}, \quad \text{(S5)}$$

where bases are denoted as $|J_z; s_z\rangle = |J, J_z\rangle\, |s, s_z\rangle$ above the matrix and $s = 1/2$. $s_z =\uparrow$ or $\downarrow$ mean $s_z = 1/2$ or $-1/2$, respectively.

The bases for the matrix in Eq. (S5) are three-particle states consisting of two holes and one electron. The matrix in Eq. (S3) can be similarly extended for the three-particle states by combining electron spins. The sum of these two Hamiltonians can be block diagonalized as follows:

$$\begin{array}{c} \begin{array}{ccccc} |-2;\downarrow\rangle & |+2;\downarrow\rangle & |+1;\uparrow\rangle & |0;\downarrow\rangle & |-1;\uparrow\rangle \end{array} \\ \begin{pmatrix} \frac{\xi}{4} + \gamma & \frac{5\xi}{4} & & & \\ \frac{5\xi}{4} & \frac{\xi}{4} - \gamma & \gamma & & \\ & \gamma & -\xi + \frac{\gamma}{2} & & \\ & & & \frac{3\xi}{2} & \frac{\sqrt{6}\gamma}{2} \\ & & & \frac{\sqrt{6}\gamma}{2} & -\xi - \frac{\gamma}{2} \\ & & & & & \ddots \end{pmatrix} \end{array}, \quad \text{(S6)}$$

where the omitted lower part for the bases in Kramers degeneracy has the same matrix elements as the upper part. The eigenvalues are obtained as

$$E_{\rm A} = E_{\rm D} = (\xi - \gamma + 5\sqrt{\xi^2 + 2\gamma\xi/5 + \gamma^2})/4, \quad \text{(S7)}$$
$$E_{\rm B} = -\xi + \gamma, \quad \text{(S8)}$$
$$E_{\rm C} = E_{\rm E} = (\xi - \gamma - 5\sqrt{\xi^2 + 2\gamma\xi/5 + \gamma^2})/4. \quad \text{(S9)}$$

For reference, we highlight here the limit case where $\gamma \ll \xi$. Eqs. (S7) and (S9) then reduce to $E_{\rm A} = E_{\rm D} \simeq 3\xi/2$ and $E_{\rm C} = E_{\rm E} \simeq -\xi - \gamma/2$. The calculated energy shifts, the sum of which yields approximate energy positions of lines #1 to #6 and the $\Gamma_7 \otimes \Gamma_7$ singlet, are summarized in Table SI. The low- and high-energy components of lines #3 and #6 are denoted by subscripts a and b, respectively. Correspondence to the exact expressions in Eqs. (S7) − (S9) is indicated in the rightest column.

TABLE SI. Energy shifts by respective interactions at the limit of small electron-hole exchange interaction ($\gamma \ll \xi$). Correspondence to the exact expressions in Eqs. (S7)−(S9) is indicated in the rightest column.

Line #	$H_{\rm so}$	$H_{\rm hh}$	$H_{\rm cf}$	$H_{\rm eh}$	$H'_{\rm cf+eh}$
$\Gamma_7 \otimes \Gamma_7$	$+4\Delta/3$	$-3\Xi_2/4$	0	0	
$6_{\rm b}$	$+\Delta/3$	$-5\Xi_1/4$	0	$+\gamma_2/2$	
$6_{\rm a}$	$+\Delta/3$	$-5\Xi_1/4$	0	$-\gamma_2$	
5	$-2\Delta/3$	$-15\Xi_0/4$	0	0	
4	$+\Delta/3$	$+3\Xi_1/4$	$+3\xi_1/2$	0	$E_{\rm A}, E_{\rm D}$
$3_{\rm b}$	$+\Delta/3$	$+3\Xi_1/4$	$-\xi_1$	$+\gamma_1$	$E_{\rm B}$
$3_{\rm a}$	$+\Delta/3$	$+3\Xi_1/4$	$-\xi_1$	$-\gamma_1/2$	$E_{\rm C}, E_{\rm E}$
2	$-2\Delta/3$	$-3\Xi_0/4$	$+3\xi_0/2$	0	$E_{\rm A}, E_{\rm D}$
$1''$	$-2\Delta/3$	$-3\Xi_0/4$	$-\xi_0$	$+\gamma_0$	$E_{\rm B}$
1	$-2\Delta/3$	$-3\Xi_0/4$	$-\xi_0$	$-\gamma_0/2$	$E_{\rm C}, E_{\rm E}$

B. Oscillator strengths

To grasp the effect of state mixing by the electron-hole exchange interaction (γ) on the oscillator strengths, we remove ξ in the off-diagonal elements by transforming

Eq. (S6) to

$$H'_{\rm cf+eh} = \begin{array}{c} \begin{array}{ccccc} |\phi'_{\rm A}\rangle & |\phi'_{\rm B}\rangle & |\phi'_{\rm C}\rangle & |\phi'_{\rm D}\rangle & |\phi'_{\rm E}\rangle \end{array} \\ \begin{pmatrix} \frac{3\xi}{2} & 0 & -\frac{\sqrt{6}\gamma}{2} & & \\ 0 & -\xi+\gamma & 0 & & \\ -\frac{\sqrt{6}\gamma}{2} & 0 & -\xi-\frac{\gamma}{2} & & \\ & & & \frac{3\xi}{2} & \frac{\sqrt{6}\gamma}{2} \\ & & & \frac{\sqrt{6}\gamma}{2} & -\xi-\frac{\gamma}{2} \\ & & & & & \ddots \end{pmatrix} \end{array}. \quad \text{(S10)}$$

The bases $|\phi'_{\rm A}\rangle$, $|\phi'_{\rm B}\rangle$, $|\phi'_{\rm C}\rangle$, $|\phi'_{\rm D}\rangle$, and $|\phi'_{\rm E}\rangle$ of this Hamiltonian are given in Table SII(a). The exact bases after diagonalization are $|\phi_{\rm A}\rangle$, $|\phi_{\rm B}\rangle$, $|\phi_{\rm C}\rangle$, $|\phi_{\rm D}\rangle$, and $|\phi_{\rm E}\rangle$ in Table SII(b), where the coefficients are expressed using $\rho_k = (E_{\rm A}-3\xi_k/2)/\sqrt{3{\gamma_k}^2/2+(E_{\rm A}-3\xi_k/2)^2}$ with $k=0$ for $\Gamma_8\otimes\Gamma_8$ states and $k=1$ for $\Gamma_7\otimes\Gamma_8$ states.

For each state, we calculated the relative oscillator strengths by the method explained in Ref. [13]. Namely, we applied the dipole operators in the second quantization to the three-particle states by expressing them as a linear combination of two-hole states times an electron state by using tables in Ref. [14]. We further decomposed the two-hole states into a pair of hole states using the Clebsch-Gordan coefficients. The hole states in Refs. [13, 14] are actually given in the "missing electron" picture or in atomic notation. For the transformation from a missing electron to a hole scheme, we changed the sign of the hole wavefunctions (with $m=-3/2$ and $1/2$) when calculating the dipole operators [15, 16]. For transitions to the $\Gamma_8\otimes\Gamma_8$ hole states, we obtained the following dipole operator:

$$\begin{aligned}\boldsymbol{\mu} = \mu_0 \Bigg[& \frac{\hat{\boldsymbol{x}}+i\hat{\boldsymbol{y}}}{\sqrt{2}}\left(-h_{\frac{3}{2}}e_{-\frac{1}{2}}+\sqrt{\frac{1}{3}}h_{\frac{1}{2}}e_{\frac{1}{2}}\right) \\ & +\frac{\hat{\boldsymbol{x}}-i\hat{\boldsymbol{y}}}{\sqrt{2}}\left(-h_{-\frac{3}{2}}e_{\frac{1}{2}}+\sqrt{\frac{1}{3}}h_{-\frac{1}{2}}e_{-\frac{1}{2}}\right) \\ & +\sqrt{\frac{2}{3}}\hat{\boldsymbol{z}}\left(-h_{-\frac{1}{2}}e_{\frac{1}{2}}+h_{\frac{1}{2}}e_{-\frac{1}{2}}\right)+\text{H.c.}\Bigg], \quad \text{(S11)}\end{aligned}$$

where μ_0 is a constant, h_m ($m=\pm3/2,\pm1/2$) and e_l ($l=\pm1/2$) are annihilation operators of a hole and electron, respectively, $\hat{\boldsymbol{x}}$, $\hat{\boldsymbol{y}}$, and $\hat{\boldsymbol{z}}$ are unit vectors along the crystal axes, and H.c. denotes Hermitian conjugate. Similarly, we derived the dipole operator for transitions from a hole in the Γ_8 state to the $\Gamma_7\otimes\Gamma_8$ two-hole states as

$$\begin{aligned}\boldsymbol{\mu} = \mu_0 \Bigg[& \frac{\hat{\boldsymbol{x}}+i\hat{\boldsymbol{y}}}{\sqrt{3}}\left(h_{\frac{1}{2}}e_{\frac{1}{2}}\right)-\frac{\hat{\boldsymbol{x}}-i\hat{\boldsymbol{y}}}{\sqrt{3}}\left(h_{-\frac{1}{2}}e_{-\frac{1}{2}}\right) \\ & -\sqrt{\frac{1}{3}}\hat{\boldsymbol{z}}\left(h_{-\frac{1}{2}}e_{\frac{1}{2}}+h_{\frac{1}{2}}e_{-\frac{1}{2}}\right)+\text{H.c.}\Bigg]. \quad \text{(S12)}\end{aligned}$$

The calculations of the squared dipole matrix elements lead to exact expressions for the oscillator strengths of lines #1 and #1′, #2 and #2′, #3$_a$ and #3′, and #4 and #4′, that are

$$A_1+A_{1'} = \frac{8}{3}+\frac{8}{\sqrt{6}}\rho_0\sqrt{1-{\rho_0}^2}-\frac{2}{3}{\rho_0}^2, \quad \text{(S13)}$$

$$A_2+A_{2'} = 2-\frac{8}{\sqrt{6}}\rho_0\sqrt{1-{\rho_0}^2}+\frac{2}{3}{\rho_0}^2, \quad \text{(S14)}$$

$$A_{3a}+A_{3'} = \frac{5}{3}-\frac{4}{\sqrt{6}}\rho_1\sqrt{1-{\rho_1}^2}+\frac{1}{3}{\rho_1}^2, \quad \text{(S15)}$$

$$A_4+A_{4'} = 2+\frac{4}{\sqrt{6}}\rho_1\sqrt{1-{\rho_1}^2}-\frac{1}{3}{\rho_1}^2, \quad \text{(S16)}$$

TABLE SII. (a) Bases for Hamiltonian, Eq. (S10). (b) Bases after diagonalizing Eq. (S10), with $\rho(=\rho_k)$ given in the text.

(a) Bases at the limit of $\gamma\to0$

$|\phi'_{\rm A}\rangle = \sqrt{\frac{1}{2}}\,|+2;\downarrow\rangle+\sqrt{\frac{1}{2}}\,|-2;\downarrow\rangle$
$|\phi'_{\rm B}\rangle = \sqrt{\frac{1}{6}}\,|+2;\downarrow\rangle-\sqrt{\frac{1}{6}}\,|-2;\downarrow\rangle+\sqrt{\frac{2}{3}}\,|+1;\uparrow\rangle$
$|\phi'_{\rm C}\rangle = \sqrt{\frac{1}{3}}\,|+2;\downarrow\rangle-\sqrt{\frac{1}{3}}\,|-2;\downarrow\rangle-\sqrt{\frac{1}{3}}\,|+1;\uparrow\rangle$
$|\phi'_{\rm D}\rangle = |0;\downarrow\rangle$
$|\phi'_{\rm E}\rangle = |-1;\uparrow\rangle$

(b) Exact bases under finite γ and ξ

$|\phi_{\rm A}\rangle = -\sqrt{1-\rho^2}\,|\phi'_{\rm A}\rangle+\rho\,|\phi'_{\rm C}\rangle$
$|\phi_{\rm B}\rangle = |\phi'_{\rm B}\rangle$
$|\phi_{\rm C}\rangle = \rho\,|\phi'_{\rm A}\rangle+\sqrt{1-\rho^2}\,|\phi'_{\rm C}\rangle$
$|\phi_{\rm D}\rangle = +\sqrt{1-\rho^2}\,|\phi'_{\rm D}\rangle+\rho\,|\phi'_{\rm E}\rangle$
$|\phi_{\rm E}\rangle = -\rho\,|\phi'_{\rm D}\rangle+\sqrt{1-\rho^2}\,|\phi'_{\rm E}\rangle$

TABLE SIII. Oscillator strengths, i.e., relative absorption intensities under a weak or strong electron-hole exchange interaction ($\gamma\to0$ or $\xi\to0$). Correspondence to the analytical expressions is indicated in the second column. The rightest column indicates theoretical intensities ($\tilde{A}_i^*$ in Table I of the main text) obtained by substituting the best-fit values of interaction parameters for boron-doped diamond to the analytical expressions.

Line#	Intensity Analytical	Intensity Calc. $\gamma\to0$ ($\rho_0,\rho_1\to0$)	Intensity Calc. $\xi\to0$ ($\rho_0,\rho_1\to\frac{2}{\sqrt{10}}$)	Intensity Fit ($\rho_1=0$, $\rho_0=0.16$)
$6_{\rm b}$	–	5/3	5/3	} 3
$6_{\rm a}$	–	4/3	4/3	
5, 5′	–	1	1	1
4, 4′	$A_4+A_{4'}$	2	8/3	2
$3_{\rm b}$	–	4/3	4/3	} 3
$3_{\rm a}$, 3′	$A_{3a}+A_{3'}$	5/3	1	
2, 2′	$A_2+A_{2'}$	2	2/3	1.50
1″	–	1/3	1/3	0.33
1, 1′	$A_1+A_{1'}$	8/3	4	3.17

respectively. The intensities depend on ρ_0 or ρ_1, thereby on the ratio of the electron-hole exchange to crystal-field interaction parameters. Intensities of other lines are not affected by the size of the interaction parameters. At the limit of $\gamma_k \to 0$ or $\xi_k \to 0$, ρ_k approaches 0 or $2/\sqrt{10}$, respectively. The calculated oscillator strengths at these limits are listed in Table SIII. The variations of intensities for lines #1−#2′ are understood as the effect of state mixing by the electron-hole exchange interaction.

The valley-orbit interaction may split the $J = 0$ state of Γ_1 symmetry with single degeneracy into three sub levels, whose effect was not included in the simplified level scheme shown in Fig. 2 of the main text. The theoretical ratio of their strengths is 1:2 ($^2\Gamma_3$:$^3\Gamma_5 \oplus {}^1\Gamma_1 = 2:4$), which is close to the experimental result of lines #5′ and #5.

C. Determination of interaction parameters

We evaluated the strengths of respective interactions by fitting the spectrum in Fig. 4(a) to Eq. (1) of the main text, where E_i and A_i were expressed as analytical forms containing interaction parameters $\Delta, \Xi_0, \xi_0, \gamma_0, \Xi_1, \xi_1, \gamma_1$, and γ_2. We used expressions in Eqs. (S7)−(S9) and (S13)−(S16) for lines #1−#4 and those in Tables SI and SIII for other lines. Valley-orbit shifts of arbitrary strengths were assumed for lines #1′, #2′, #3′, #4′, and #5′. We set $\gamma_1 = \gamma_2 = 0$ because no exchange splitting was observed in lines #3 and #6, and fixed w_i at the values given in Table I of the main text. The best-fit values of the interaction parameters are summarized in Table SIV. All interaction parameters were found to be smaller in the $\Gamma_7 \otimes \Gamma_8$ triplet than in the $\Gamma_8 \otimes \Gamma_8$ triplet. The oscillator strengths were then calculated (using $\rho_0 = 0.16$ and $\rho_1 = 0$) as listed in the rightest column of Table SIII. The same values are plotted in Fig. 4(b) of the main text, which shows excellent agreement with observations.

The spin-orbit splitting was obtained by the fit to be $\Delta = 14.3 \pm 0.1$ meV. Regarding the hole-hole exchange interaction, the large amplitude of Ξ_0 indeed provides the nesting of lines #5′ and #5 into the $\Gamma_7 \otimes \Gamma_8$ triplet. We found that the amplitude of the interaction parameter for the $\Gamma_7 \otimes \Gamma_8$ states, $|\Xi_1|$, is about half that for the $\Gamma_8 \otimes \Gamma_8$ states, $|\Xi_0|$. Applying this tendency, $|\Xi_2|$ for the $\Gamma_7 \otimes \Gamma_7$ states is expected to be smaller than $|\Xi_1|$. Setting the limits $|\Xi_2| < |\Xi_1|$ and $\Xi_2 < 0$ on Ξ_2 predicts the position of the $\Gamma_7 \otimes \Gamma_7$ singlet in the range from 25.1 to 26.5 meV ($= 2\Delta - 3\Xi_2/4 + 3\Xi_0/4 + \xi_0 + \gamma_0/2 - \Delta_a$) higher than that of line #1. The subtraction of $\Delta_a = 2$ meV is to take the transition from the Γ_7 acceptor, which does not require relaxation of the hole spin. This transition is expected to be weak due to the single level degeneracy ($g = 1$) of the final state and thermal broadening when the initial state is populated. As shown in Fig. S3, this transition was not observed in the experimental spectra.

TABLE SIV. Interaction parameters for the acceptor-bound exciton in diamond, determined by the fit to experimental data at 2 K.

Interaction	Two-hole state	Best-fit value [meV]
Spin-orbit		$\Delta = 14.3$
Hole-hole exchange	$\Gamma_8 \otimes \Gamma_8$	$\Xi_0 = -4.1$
	$\Gamma_7 \otimes \Gamma_8$	$\Xi_1 = -1.9$
Crystal-field potential	$\Gamma_8 \otimes \Gamma_8$	$\xi_0 = 1.3$
	$\Gamma_7 \otimes \Gamma_8$	$\xi_1 = 0.3$
Electron-hole exchange	$\Gamma_8 \otimes \Gamma_8$	$\gamma_0 = 0.5$
	$\Gamma_7 \otimes \Gamma_8$	$\gamma_1 = \gamma_2 = 0$

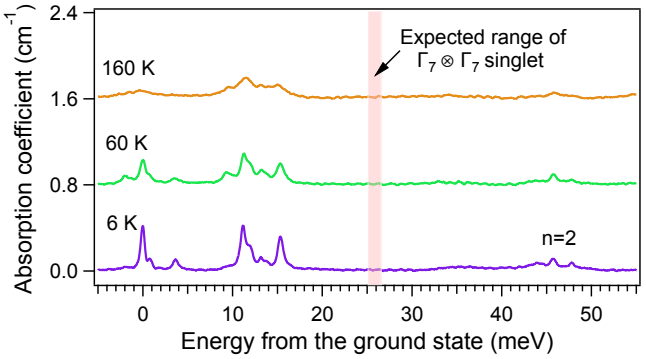

FIG. S3. Absorption spectra of boron-doped diamond obtained at different temperatures indicating the absence of transition to $\Gamma_7 \otimes \Gamma_7$ singlet. The $n = 2$ components correspond to excited quasiexciton states of the bound exciton [17].

Finally, we revisit past studies on the fine structure of bound excitons in semiconductors to provide a general view. Table SV compares the interaction strengths extracted for acceptor-bound excitons in semiconductors of different crystal structures. Here, we chose to list values of energy splitting rather than interaction parameters, to avoid possible confusion due to different notations of the latter depending on the authors. Note that the energy splittings may contain some additional factors to the interaction parameters in Table SIV. The case of the hole-hole exchange interaction is not straightforward; The *cubic* term of the hole-hole exchange interaction (with the strength denoted by $C^2_{\rm hh}$ [11] and called *crystal-field potential* elsewhere denoted by ξ) contains energy offsets, which have *spherical* symmetry. Adding this contribution to the spherical part of the hole-hole exchange interaction leads to the relation, $\Xi = C^1_{\rm hh} + \frac{41}{10} C^2_{\rm hh}$. In Table SV, the energy splittings in parentheses were derived based on the $C^1_{\rm hh}$ and $C^2_{\rm hh}$ values reported in Ref. [11]. For silicon and GaAs, we also analyzed the data presented in literature [13, 18] and obtained the energy splittings given without parentheses.

These conversions facilitate a direct comparison of respective interaction strengths in group-IV elemental and III-V or II-VI compound semiconductors. There is a trend that the splitting becomes large with increasing localization energy $E_{\rm loc}$ of the exciton on an acceptor (the

TABLE SV. Comparison of energy splittings in acceptor-bound excitons by the interactions considered in our model. Values determined by the present work in diamond are shown in bold font. The spin-orbit splitting is $\Delta = \mathbf{14.3}$ meV in boron-doped diamond (C:B). Bandgap E_g, acceptor Bohr radius a_B, localization energy $E_{\rm loc}$ of the exciton at the acceptor, and the two-hole angular momentum J of the ground state (GS) are also listed. For wurtzite cases, (A) and (B) denote A- and B-valence bands, respectively.

Material (two-hole state)	Bandgap E_g [eV]	Radius a_B [nm]	Loc. energy $E_{\rm loc}$ [meV]	Hole-hole exchange $3\Xi_0$ $(3C^1_{\rm hh} + \frac{123}{10}C^2_{\rm hh})$ [meV]	Crystal-field potential $\frac{5}{2}\xi$ $(-3C^2_{\rm hh})$ [meV]	Electron-hole exch. $\frac{3}{2}\gamma$ [meV]	GS J
Diamond							
C:B ($\Gamma_8 \otimes \Gamma_8$)	5.50[a]	0.52[b]	49[d]	$3\Xi_0 = \mathbf{-12.3}$	**3.3**	**0.7**	**2**
C:B ($\Gamma_7 \otimes \Gamma_8$)				$2\Xi_1 = \mathbf{-3.8}$	**0.9**	**0**	**2**
Si:acceptor		2.55[c]		–	0.3[f]	–	
Si:B			4.2 ± 0.2[e]	$(-0.001)^\dagger$	$(-0.081)^\S$	$-0.056^\#$	2
Si:Al	1.12[a]		5.2 ± 0.2[e]	$1.2^\star$ $(1.0)^\dagger$	$0.23^\star$ $(0.30)^\S$	–	0
Si:Ga			6.0 ± 0.2[e]	$1.6^\star$ $(1.3)^\dagger$	$0.38^\star$ $(0.45)^\S$	–	0
Si:In			14.0 ± 0.2[e]	$4.5^\star$ $(4.4)^\dagger$	$3.3^\star$ $(3.09)^\S$	–	0
Zinc blende							
CdTe:Li, Na	1.475[a]	2.72[c]	7.0, 7.1[f]	not observed[f]	$-0.28^\$$	$-0.015^\$$	2
InP:Zn	1.344[a]	4.12[c]	3.6[g]	$-0.34^{\ddagger,g}$	$-0.23^{f,g}$	w/o noticeable[g]	2
GaAs:Zn	1.424[a]	5.08[c]	2.5[h]	$-0.55^\diamond$	$-0.17^\diamond$, $-0.18^{f,g,m}$	$\lvert\frac{3}{2}\gamma\rvert < 0.033^\diamond$	2
Wurtzite							
CdS:Li,V-Al (A)	2.482[a]	–	18.09[i]	$\Xi_0 = 3.4 \pm 0.2$[l]	$\xi_0 = 0.2 \pm 0.1$[l]	$\gamma_0 = -0.4 \pm 0.1$[l]	0
CdS:Li,V-Al (B)	2.496[a]	–	20.90, 19.35[i]	–	–	–	
GaN:Mg (A)	3.44[a]	–	11.5[j]	–	–	–	
AlN:Mg (A)	6.13[a]	–	23.2[k]	–	–	–	

[a] Room temperature values from Ref. [19] [b] Ref. [20] [c] Ref. [21] [d] Ref. [22] [e] Ref. [23] [f] Ref. [10] [g] Ref. [24]
[h] Ref. [25] [i] Ref. [26] [j] Ref. [27] [k] For the crystal-field split-off hole, Ref. [28] [l] Ref. [8] [m] Ref. [29]
* Estimated by analyzing the spectra in Ref. [18].
† Calculated from $C^1_{\rm hh}$ and $C^2_{\rm hh}$ given in Ref. [11].
‡ The splitting is denoted as γ in Ref. [24].
$^\diamond$ Estimated by analyzing the spectra in Ref. [13], where acceptor species are unspecified.
§ Calculated from $C^2_{\rm hh}$ given in Ref. [11].
$^\$$ $\xi = -0.11$ and $\gamma = -0.01$ are given in Ref. [10].
$^\#$ $\gamma = -0.037$ is given in Ref. [11].

spin-orbit splitting is not discussed as only available for diamond). This is consistent with the linear dependency [30] of the hole-hole exchange splitting on the acceptor ionization energy $E_{\rm io}$, and thus on the localization energy of the exciton on the acceptor $E_{\rm loc} \sim 0.12E_{\rm io}$ [22]. The negative values of Ξ are common among diamond and the excitons bound to shallow acceptors in CdTe:Li [10], CdTe:Na [10], InP:Zn [24], and GaAs [29]. The ground states are thus derived from the $J = 2$ two-hole states rather than from the $J = 0$ states as reported for excitons bound to deep acceptors in Si:Al, Si:Ga, Si:In [18]. The crystal-field splitting is known to scale with the inverse effective Bohr radius ($1/a_B \propto \sqrt{E_{\rm loc}}$ [21]) for InP, GaAs, Si:Al, Si:Ga [24]. The 0.52 nm radius for boron-doped diamond [20] predicts $\frac{5}{2}\xi = 1.6$ meV, in between the observations of $\frac{5}{2}\xi_0$ =3.3 meV and $\frac{5}{2}\xi_1 = 0.9$ meV. The electron-hole exchange splitting found for the $\Gamma_8 \otimes \Gamma_8$ two-hole states in diamond is large compared to those reported for compound semiconductors.

To conclude, the high localization energy of excitons in diamond is the fundamental physical reason why the energy splittings in the bound-exciton fine structure are largest among those reported in semiconductors. This unique property of diamond enabled our definite level assignment and the first determination of the spin-orbit splitting for acceptor-bound excitons in semiconductors. Diamond is the only cubic semiconductor clearly fulfilling the condition of $E_{\rm loc} > \Delta$. This leads to the appearance of the *split-off* hole band in the bound-exciton fine structure, similarly to the case of wide-bandgap semiconductors of hexagonal structures.

[1] R. Issaoui, J. Achard, A. Tallaire, F. Silva, A. Gicquel, R. Bisaro, B. Servet, G. Garry, and J. Barjon, Evaluation of freestanding boron-doped diamond grown by chemical

vapour deposition as substrates for vertical power electronic devices, Appl. Phys. Lett. **100**, 122109 (2012).
[2] Y. Kubo, S. Temgoua, R. Issaoui, J. Barjon, and N. Naka, Radiative lifetime of boron-bound excitons in diamond, Appl. Phys. Lett. **114**, 132104 (2019).
[3] C. D. Clark, P. J. Dean, and P. V. Harris, Intrinsic edge absorption in diamond, Proc. R. Soc. London. Ser. A. Math. Phys. Sci. **277**, 312 (1964).
[4] K. Konishi and N. Naka, Phonon-assisted excitonic absorption in diamond, Phys. Rev. B **104**, 125204 (2021).
[5] H. Kim, R. Vogelgesang, A. K. Ramdas, S. Rodriguez, M. Grimsditch, and T. R. Anthony, Electronic Raman and infrared spectra of acceptors in isotopically controlled diamonds, Phys. Rev. B **57**, 15315 (1998).
[6] D. G. Thomas and J. J. Hopfield, Optical Properties of Bound Exciton Complexes in Cadmium Sulfide, Phys. Rev. **128**, 2135 (1962).
[7] R. Sauer, H. Sternschulte, S. Wahl, K. Thonke, and T. R. Anthony, Revised Fine Splitting of Excitons in Diamond, Phys. Rev. Lett. **84**, 4172 (2000).
[8] B. Gil, P. Bigenwald, P. P. Paskov, and B. Monemar, Internal structure of acceptor-bound excitons in wide-band-gap wurtzite semiconductors, Phys. Rev. B **81**, 085211 (2010).
[9] S. Sugano, Y. Tanabe, and H. Kamimura, *Multiplets of Transition-Metal Ions in Crystals* (Academic Press, 1970).
[10] E. Molva and L. S. Dang, Magneto-optical study of Li and Na acceptor bound excitons in CdTe: Fine structure and cubic crystal-field effect, Phys. Rev. B **32**, 1156 (1985).
[11] V. A. Karasyuk, A. G. Steele, A. Mainwood, E. C. Lightowlers, G. Davies, D. M. Brake, and M. L. W. Thewalt, Ultrahigh-resolution photoluminescence studies of excitons bound to boron in silicon under uniaxial stress, Phys. Rev. B **45**, 11736 (1992).
[12] G. E. Pikus and G. L. Bir, Exchange Interaction In Excitons In Semiconductors, Sov. Phys. JETP **33**, 108 (1971).
[13] T. Karin, R. J. Barbour, C. Santori, Y. Yamamoto, Y. Hirayama, and Kai-Mei C. Fu, Radiative properties of multicarrier bound excitons in GaAs, Phys. Rev. B **91**, 165204 (2015).
[14] G. F. Koster, J. O. Dimmock, R. G. Wheeler, and H. Statz, *Properties of the thirty-two point groups* (MIT Press, 1963).
[15] T. Morgan, Oscillator strengths for electron-hole complexes (A^0X), J. Phys. C: Solid State Phys. **10**, L131 (1977).
[16] B. Hönerlage and I. Pelant, *Symmetry and Symmetry-Breaking in Semiconductors*, PUBDB-2021-02091 (Springer, 2018).
[17] Y. Kubo, M. Takahata, S. Temgoua, R. Issaoui, J. Barjon, and N. Naka, Phonon-assisted transitions of bound excitons in diamond: Analysis by mirror symmetry, Phys. Rev. B **101**, 205204 (2020).
[18] K. R. Elliott, G. C. Osbourn, D. L. Smith, and T. C. McGill, Bound-exciton absorption in Si:Al, Si:Ga, and Si:In, Phys. Rev. B **17**, 1808 (1978).
[19] O. Madelung, *Semiconductors: Data Handbook* (Springer, 2004).
[20] T. Shimomura, Y. Kubo, J. Barjon, N. Tokuda, I. Akimoto, and N. Naka, Quantitative relevance of substitutional impurities to carrier dynamics in diamond, Phys. Rev. Mater. **2**, 094601 (2018).
[21] A. Baldereschi and N. O. Lipari, Spherical Model of Shallow Acceptor States in Semiconductors, Phys. Rev. B **8**, 2697 (1973).
[22] J. Barjon, Luminescence Spectroscopy of Bound Excitons in Diamond, Phys. Status Solidi A **214**, 1700402 (2017).
[23] M. Vouk and E. Lightowlers, A high resolution investigation of the recombination radiation from Si containing the acceptors B, Al, Ga, In and Tl, J. Lumin. **15**, 357 (1977).
[24] H. Mathieu, J. Camassel, and F. B. Chekroun, Stress effects on excitons bound to neutral acceptors in InP, Phys. Rev. B **29**, 3438 (1984).
[25] Y. Takeuchi, Y. Makita, K. Kudo, T. Nomura, H. Tanaka, K. Irie, and N. Ohnishi, Observation of new common emissions in GaAs produced by ion implantation of four acceptor impurities, Appl. Phys. Lett. **48**, 59 (1986).
[26] J. Gutowski, Electronic and vibronic states of the acceptor—bound-exciton complex (A^0, X) in CdS. II. Determination of the fine structure of the (A^0, X_B) electronic states by high-resolution excitation spectroscopy, Phys. Rev. B **31**, 3611 (1985).
[27] A. Wysmolek, M. Potemski, R. Stepniewski, J. Lusakowski, K. Pakula, J. M. Baranowski, J. Martinez, P. Wyder, I. Grzegory, and S. Porowski, Polarised Magnetoluminescence of Excitons in Homoepitaxial GaN Layers, Phys. Status Solidi B **216**, 11 (1999).
[28] R. Ishii, A. Yoshikawa, M. Funato, and Y. Kawakami, Revisiting the substitutional Mg acceptor binding energy of AlN, Phys. Rev. B **108**, 035205 (2023).
[29] M. Schmidt, T. N. Morgan, and W. Schairer, Stress effects on excitons bound to shallow acceptors in GaAs, Phys. Rev. B **11**, 5002 (1975).
[30] P. J. Dean, W. F. Flood, and G. Kaminsky, Absorption due to Bound Excitons in Silicon, Phys. Rev. **163**, 721 (1967).